

Supplementary information

1 UAV DTM processing workflow and DBCA LiDaR details

In order to recover the surface deformation envelope associated with the events, aerial photographs were acquired with a DJI Phantom 4 UAV in an approximately 500 m-wide swath along an approximately 2 km length of the scarp produced in the September event. A ~2 km-long cross-line was also flown, extending eastward from the scarp across the region of most significant surface deformation indicated in the InSAR data (Figure 3). Flights were planned in the Map Pilot software (version 3.0.0) provided by Drones Made Easy (<https://support.dronesmadeeasy.com/hc/en-us/categories/200739936-Map-Pilot-for-DJI>). The 1144 images were captured in RAW format from an average elevation above the take-off point of 100 m, with 75% overlap in the forward and sideward directions, achieving an effective ground sampling distance of ~5.25 cm. Seventeen ground control points (GCPs) were deployed within the 1.75 km² mission area, and their locations were surveyed to better than 0.03 m accuracy in the horizontal and 0.06 m accuracy in the vertical using an Altus RTK GPS system. Due to the size of the area being captured, the coverage was acquired over two days.

The image dataset was processed using a Structure-from-Motion (SfM) and multi-view stereo approach, implemented in the software Agisoft Photoscan Pro 1.4.3 (Agisoft LCC). Initial image alignment and production of a sparse point cloud was achieved using the approximate 3D position, roll, pitch and yaw of the UAV captured by the UAV's on-board GPS and an inertial measurement unit. The GCPs were then manually identified on the images and their co-ordinates imported. The co-ordinates of the GCPs were used to refine the camera calibration parameters, and to optimise the geometry of the sparse point cloud. Multi-view stereo image matching algorithms (Seitz et al., 2006), implemented in Agisoft Photoscan Pro 1.4.3, were then applied to densify the sparse point cloud. The resulting dense point cloud achieved a standard deviation of the location differences between it and the control points of 0.09 m in the horizontal and 0.01 m in the vertical, which is comparable to other studies using similar GCP densities (e.g. Gindraux et al., 2017). Several studies of factors impacting local photogrammetry-derived DSM accuracy (e.g. Gindraux et al., 2017; Tonkin and Midgley, 2016) report a vertical accuracy decrease of ~0.1 m for every 100 m increase in the distance to the closest GCP. In extreme cases this can result in a 'bowl' or 'dome' effect (e.g. Ouédraogo et al., 2014). In our study the maximum distance from a control point is in the order of 200-300 m.

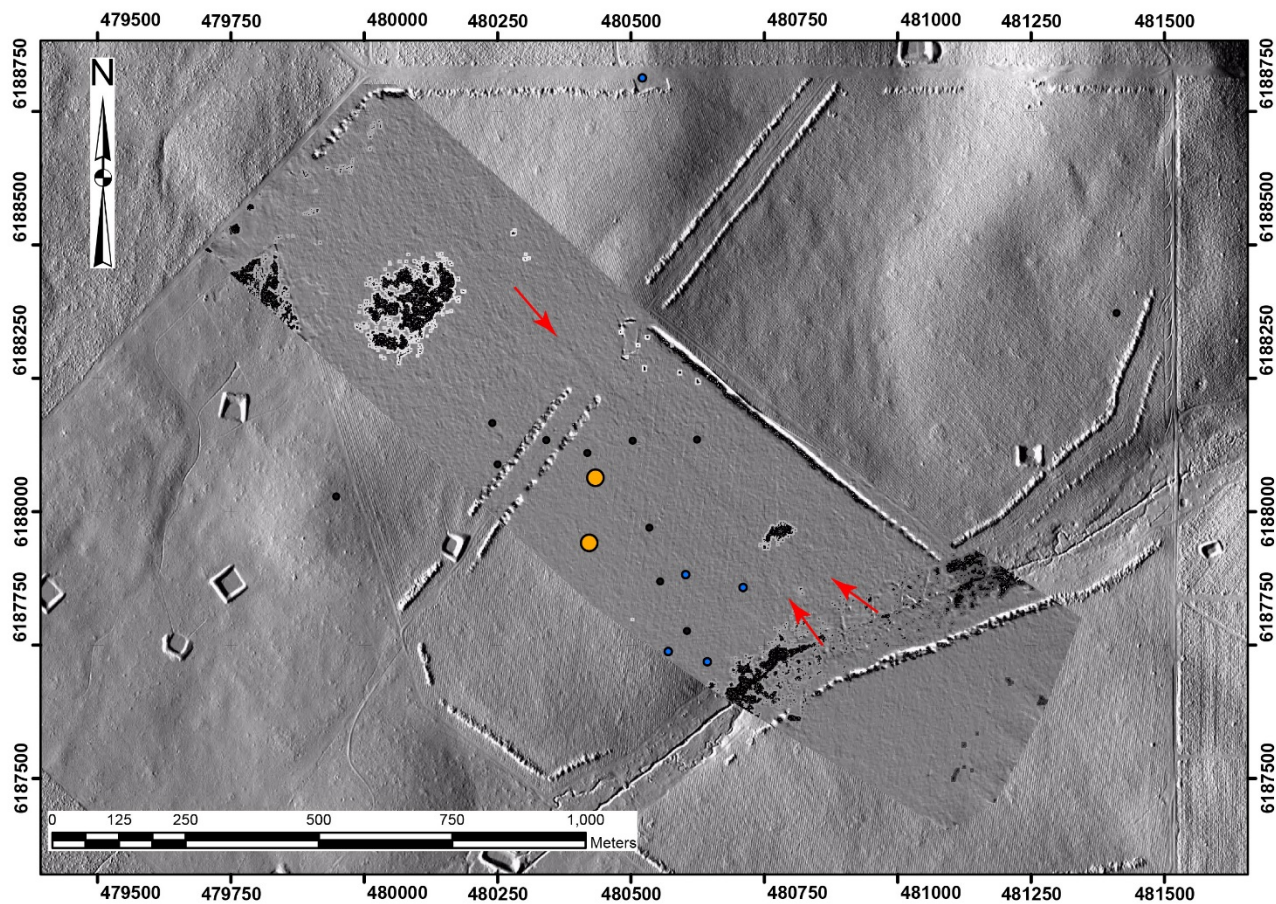
The dense point cloud was exported to the American Society for Photogrammetry and Remote Sensing (ASPRS) LAS format and classified into ground and non-ground points using the Cloth Simulation Filtering algorithm (Zhang et al., 2016; Serifoglu Yilmaz et al., 2018) implemented in the open source software package CloudCompare (<https://www.danielgm.net/cc/>). Points comprising the ground class were then re-imported into Photoscan, and a 6 cm-resolution Digital Terrain Model (DTM) was

generated. The DTM was used within the software to produce an orthophoto, then exported to geotiff format for further analysis.

In January 2012, the Western Australia Government Department of Biodiversity, Conservation and Attractions (DBCA) acquired a 1 m gridded LiDAR DTM covering the study area. The average magnitude of the uncertainties associated with the elevation values for this dataset is reported as 0.063 ± 0.074 m. The elevation values from a subset of the LiDAR were subtracted from the ground class DTM generated in this study, to produce a DTM of difference (DoD, Williams, 2012). Voids in the DoD were filled using the ESRI ArcGIS *focal statistics tool* (null values are filled with the mean value within a rectangular neighbourhood of 50 cells dimension).

Change in land use from forestry to pasture in the time between acquisition of the LiDAR and UAV datasets has resulted in the introduction of several artefacts into the differenced DEM. For example, forestry practice involved the construction of numerous parallel furrows up to 0.1 – 0.2 m high and at 3 – 4 m spacing, into which pine trees were planted. The relief on these furrows has significantly eroded in the 6.5 years between the acquisition of the datasets. Several dams have also been constructed, one of which resulted in the modification of a wetland. Despite these sources of ‘cultural noise’, the vertical displacement envelope resulting from the September earthquake was able to be recovered from the DoD, with an accuracy of approximately 0.1 - 0.2 m.

A third UAV mission covered the southern extent of surface deformation indicated in the InSAR imagery (Figures 3, S1). Six GCPs were deployed within the 0.86 km² mission area, and their locations were surveyed to better than 0.02 m accuracy in the horizontal and 0.04 m accuracy in the vertical using an Altus RTK GPS system. A DoD was calculated using the same methodology above. The DoD shows the faint but continuous trace of a rupture that is everywhere less than 5 cm in height. While this displacement magnitude is consistent with the estimates using the unwrapped InSAR (Figure 6b), the orientation of the rupture at this location, sub-parallel to the maximum compression direction of the crustal stress field (Rajabi et al., 2017), suggests that horizontal motion may have been dominant. The vertical UAV signature might result in part from horizontal displacement of furrows associated with the former forestry land-use.



55 **Figure S1: UAV DoD for the southern terminal structure. Subtle scarp with <5 cm vertical displacement is indicated by red arrows (GDA94/MGA50).**

Aftershock relocation

Following the Mw 5.3 earthquake near Lake Muir, Western Australia, 884 earthquakes from 16 September, 2018 to 23 November, 2018 were recorded on stations from the permanent ANSN network and from five rapid deployment aftershock
 60 kits temporarily installed in the epicentral region. The original locations of these events were located using SeisComP3 seismological software and the LocSAT location algorithm. P- and S-wave arrival times were manually picked and reviewed by on-duty seismic analysts.

To better constrain the location and pattern of aftershocks, events from this dataset were relocated using the HypoDD double-difference relative location algorithm (Waldhauser and Ellsworth, 2000), and implemented with the corresponding software,
 65 HypoDDpy (Krischer, 2015). The HypoDD algorithm minimizes errors in hypocentral locations that are commonly attributed to uncertainties in earth structure along the event-station ray path. The algorithm works by first establishing a network of differential P- and S-wave travel times between two proximally located hypocentres that share a minimum number of P- and

S-phase arrivals at common stations. This network of events is determined through initial parameterization using the Ph2dt program (Table S1). This parameterization includes setting a maximum separation distance in kilometres (MAXSEP), a minimum number of phase pairs (MINLNK), and a maximum number of neighbouring events (MAXNGH). To establish strong links between events, Waldhauser (2001) recommends at least eight observations (MINOBS) for each event pair. Table S1 outlines the initial parameters used in the Ph2dt program for the Lake Muir earthquakes. MAXDIST specifies the distance between the event and station in km, and was set to a default value of 100, which includes all stations capable of recording the smaller-magnitude aftershocks in the Lake Muir area. Only events from the original dataset that meet this initial criteria are used in the HypoDD inversion. As a result, catalogue P- and S-wave data from 470 events were included in the final relocation.

MAXDIST	MAXSEP	MAXNGH	MINLNK	MINOBS
100	1	100	8	8

Table S1 Ph2dt input Parameters

Once events are linked together with the Ph2dt program and networks of event pairs are generated, HypoDD groups these events into clusters and then minimizes the travel-time residuals by adjusting the spatial difference of the hypocentres relative to the other hypocentres within the cluster. The double-difference travel-time residual is the difference between the observed and theoretical travel times for each event pair. The source of the P- or S-wave travel time differences of two events at one station can then be attributed to a spatial offset between the hypocentres, since the ray paths between the earthquake source and the seismic station are assumed to be similar. Theoretical travel times are calculated using a 1-D P-wave velocity model, which is derived from Dentith et al. (2000) and Salmon et al. (2012) and incorporates a shallow, low-velocity sediment layer. The VP/VS ratio was set to 1.73.

Depth (km)	0	0.1	5.0	10	15	20	25
P-wave Velocity (km/s)	1.11	5.95	6.20	6.27	6.37	6.57	6.97

Table S2 1-D P-wave velocity model

The double-difference travel-time residuals are minimized by weighted least squares. The Singular Value Decomposition (SVD) inversion method was chosen as the preferred inversion method, because SVD can examine smaller clusters of events and can also produce meaningful three-dimensional hypocentre relocation error estimates (2001). Before running the inversion, the original earthquake locations were separated into four different datasets, shown by the dashed boxes in Figure 1. The events were split to regulate the size of the relocation inversion problems to be solved. The aftershocks in subset A were restricted to magnitudes $ML \geq 1.0$, since the total number of events near the focus of the 16 September mainshock would

be too large for the SVD inversion method. This magnitude threshold also ensures that the earthquakes are clearly recorded by both the local Lake Muir stations and by regional ANSN stations. Subset D was relocated separately, because these aftershocks temporally relate to the 16 September mainshock and are spatially related to the southern extent of surface rupture. The number of earthquakes and delay times for each subset A-D are shown in Table S3.

Data Subset	Earthquake Counts	P- Delay Times	S- Delay Times
A	106	7401	7314
B	182	8611	9289
C	103	5287	5290
D	18	279	294

Table S3 Earthquake and delay time counts

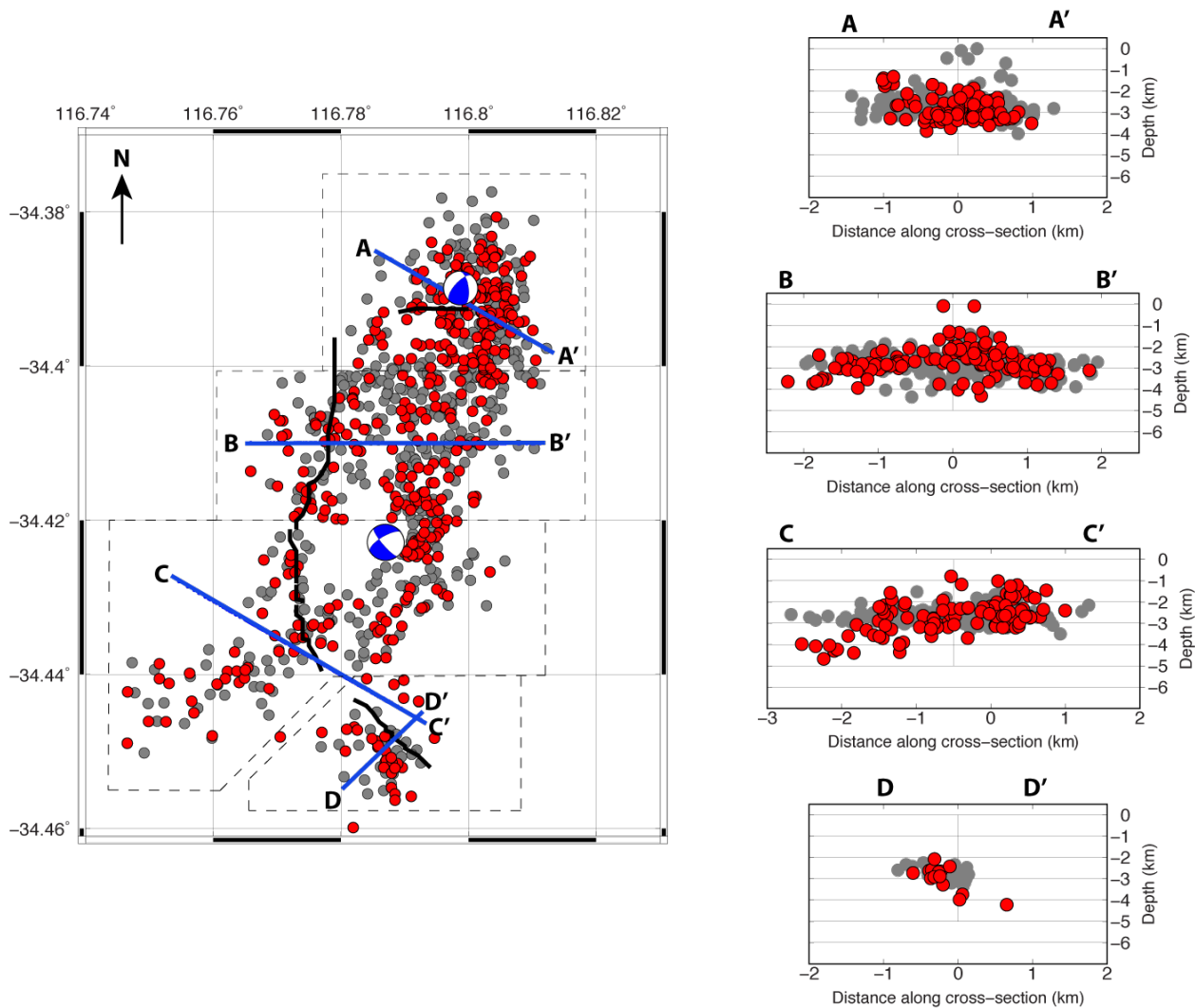
105

Within subset A, the A-A' cross-section is oriented approximately normal to the strike direction of the 16 September, 2018 focal mechanism. These events relocate to depths between 1 and 4 km (Figure S2). There is no clearly defined dip angle to this event cluster. Within subset B and along the B-B' cross-section, which is normally oriented to the discrete surface rupture, the earthquakes are also clustered between 1 and 4 km depth. East of the cross-section centre, the aftershocks dip $\sim 30^\circ$ to the east. The C-C' cross-section is oriented NW-SE: normal to the north-east trending nodal plane of 11 November, 2018 focal mechanism. The epicentres in subset C that linearly trend to the northeast, relocate along a steeply-dipping plane to the north-west. The remaining aftershocks within subset C are constrained to depths of $\sim 1-3$ km and show no defined dip direction. Lastly, within the small subset D, the events relocate ~ 300 m south-west of the observed fault rupture and are constrained to $\sim 2-3$ km depth (Figure S2). The mean east-west (EX), north-south (EY), and vertical (EZ) location errors with one standard deviation are displayed in Table S4.

115

Data Subset	Mean EX $\pm 1\sigma$	Mean EY $\pm 1\sigma$	Mean EZ $\pm 1\sigma$
A	47 \pm 30	86 \pm 74	126 \pm 134
B	72 \pm 72	137 \pm 147	215 \pm 242
C	55 \pm 30	92 \pm 72	306 \pm 255
D	94 \pm 59	165 \pm 66	523 \pm 236

Table S4 Least squares error estimates (m)



120

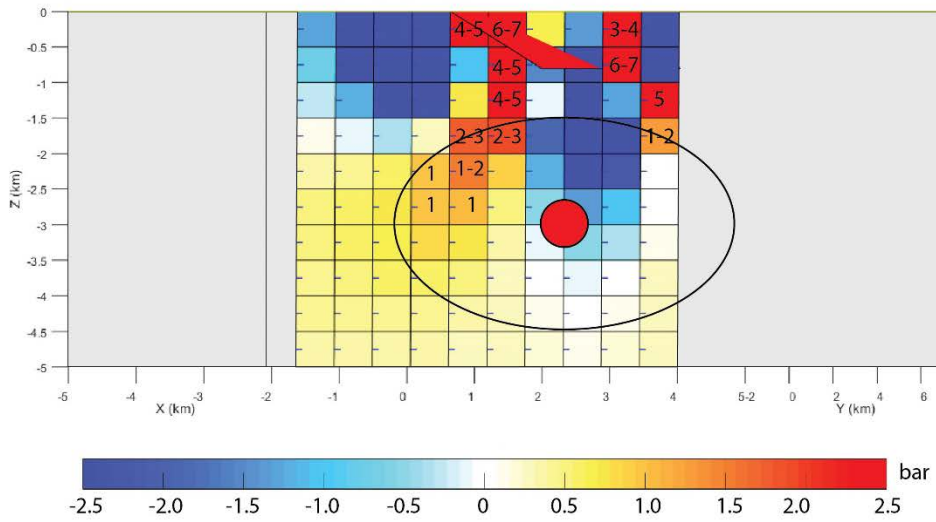
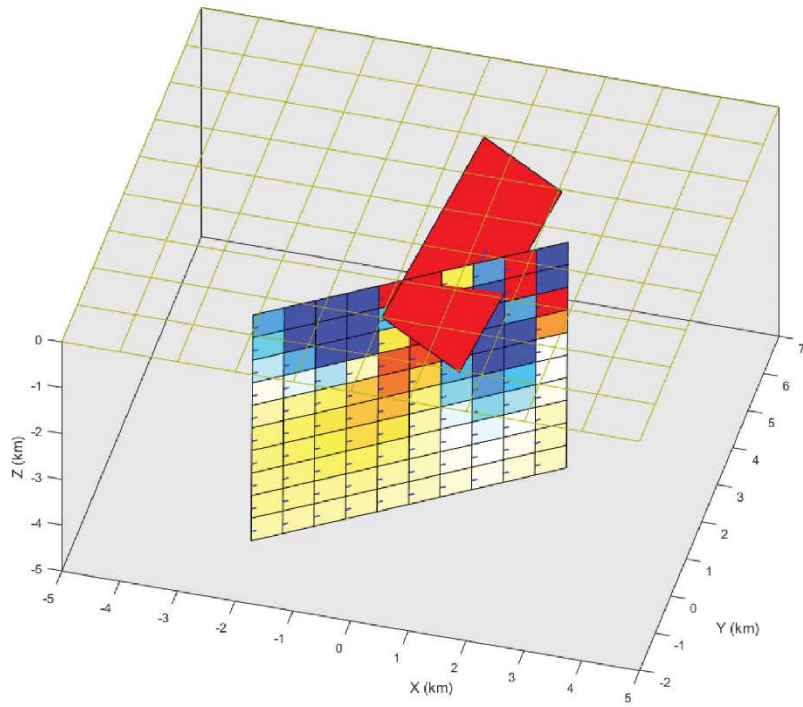
Figure S2: Relatively relocated aftershock map and cross-sections near Lake Muir, Western Australia. Grey circles represent the original earthquake locations, and the red circles represent the relocated earthquakes. Dashed boxes indicate the geographical boundaries for the data subsets A-D. Original and relocated earthquakes are projected onto the blue cross-section lines. The length of each cross-section is defined to include all original and relocated epicentres from each subset. The black lines mark the observed surface rupture from the 16 September earthquake. The focal mechanisms generated by the USGS for the 16 September M_w 5.3 and 11 November M_w 5.2 events are also plotted in map view.

125

Coulomb Stress modelling

130

- When slip occurs on a fault (the ‘source’ fault) stress is imparted to the surrounding crust and faults (‘receiver’ faults). In Coulomb stress modelling (e.g. Lin and Stein, 2004;Toda et al., 2005;Toda et al., 2011), fault displacements in the elastic half-space are used to calculate a 3D strain field, which is multiplied by the elastic stiffness to derive stress changes. Stress changes might be used to understand the distribution of aftershocks resulting from an event, or the static stress changes caused by displacement on a ‘source’ fault can be resolved onto ‘receiver’ faults to investigate whether they are promoted towards failure. The shear stress increase or decrease is dependent on the position, geometry, and slip of the source fault and on the position and geometry of the receiver fault, including its rake. The normal stress change (clamping or unclamping) is independent of the receiver fault rake (Toda et al., 2011).
- 135
- 140 Toda et al. (2011) use the Coulomb failure criterion, $\Delta\sigma_f = \Delta\tau_s + \mu' \Delta\sigma_n$, in which failure is hypothesized to be promoted when the Coulomb stress change is positive. Here, $\Delta\sigma_f$ is the change in failure stress on the receiver fault caused by slip on the source fault(s), $\Delta\tau_s$ is the change in shear stress (reckoned positive when sheared in the direction of fault slip), $\Delta\sigma_n$ is change in normal stress (positive if the fault is unclamped), and μ' is the effective coefficient of friction on the fault.
- 145 The source fault was parametrised as follows: length = 5 km, strike = 5° , dip = 30° , dip slip = 0.6 m, strike slip = 0.0 m, rake = 90° , top of rupture = 0 km, bottom of rupture = 0.8 km, co-efficient of friction (μ') = 0.6. The receiver fault was parametrised as follows: length = 5 km, strike = 215° , dip = 89° , dip slip = 0.0 m, strike slip = 0.0 m, rake = 180° , top of rupture = 0 km, bottom of rupture = 5.0 km.
- 150 The Coulomb stress change consequent of the Lake Muir September M_W 5.3 reverse fault rupture was resolved for dextral strike slip events parallel to the plane of the November M_W 5.2 strike-slip rupture (Figure S3). This calculation shows that the plane of the November rupture was brought closer to failure over approximately half of its area.



155

Figure S3: Coulomb stress change resulting from the September event resolved for dextral strike-slip events onto the plane of the November rupture. Stress increase values are shown in bars. The location and uncertainty ellipse of the hypocentre for the November event is shown.

References

- 160 Agisoft LCC: . Agisoft PhotoScan Pro 1.4.3. Available online: <http://www.agisoft.com> (accessed November 2018).
Dentith, M. C., Dent, V. F., and Drummond, B. J.: Deep crustal structure in the southwestern Yilgarn Craton, Western Australia, *Tectonophysics*, 325, 227-255, 2000.
Gindraux, S., Boesch, R., and Farinotti, D.: Accuracy Assessment of Digital Surface Models from Unmanned Aerial Vehicles' Imagery on Glaciers, *Remote Sensing*, 9, 186, 2017.
- 165 Krischer, L.: hypoDDpy: hypoDDpy 1.0 Zenodo, 2015.
Lin, J., and Stein, R. S.: Stress triggering in thrust and subduction earthquakes and stress interaction between the southern San Andreas and nearby thrust and strike-slip faults, *Journal of Geophysical Research: Solid Earth*, 109, doi:10.1029/2003JB002607, 2004.
Ouédraogo, M. M., Degré, A., Debouche, C., and Lisein, J.: The evaluation of unmanned aerial system-based photogrammetry and terrestrial laser scanning to generate DEMs of agricultural watersheds, *Geomorphology*, 214, 339–355, 2014.
- 170 Rajabi, M., Tingay, M., Heidbach, O., Hillis, R., and Reynolds, S.: The present-day stress field of Australia, *Earth-Science Reviews*, 168, 165-189, 10.1016/j.earscirev.2017.04.003, 2017.
Salmon, M., Kennett, B. L. N., and Saygin, E.: Australian Seismological Reference Model (AuSREM): crustal component, *Geophysical Journal International*, 192, 190-206, 10.1093/gji/ggs004 %J *Geophysical Journal International*, 2012.
- 175 Seitz, S. M., Curless, B., Diebel, J., Scharstein, D., and Szeliski, R.: A comparison and evaluation of multi-view stereo reconstruction algorithms, In *Proceedings of the 2006 IEEE Computer Society Conference on Computer Vision and Pattern Recognition (CVPR'06)*, New York, NY, USA, 17–22 June 2006, 1, 2006.
Serifoglu Yilmaz, C., Yilmaz, V., and Güngör, O.: Investigating the performances of commercial and non-commercial software for ground filtering of UAV-based point clouds, *International Journal of Remote Sensing*, 39, 5016-5042, 10.1080/01431161.2017.1420942, 2018.
- 180 Toda, S., Stein, R. S., Richards-Dinger, K., and Bozkurt, S. B.: Forecasting the evolution of seismicity in southern California: Animations built on earthquake stress transfer, 110, 10.1029/2004jb003415, 2005.
Toda, S., Stein, R. S., Sevilgen, V., and Lin, J.: Coulomb 3.3 Graphic-Rich Deformation and Stress-Change Software for Earthquake, Tectonic, and Volcano Research and Teaching — User Guide, USGS Open File Report, 2011-1060, 63p, 2011.
- 185 Tonkin, T. N., and Midgley, N. G.: Ground-Control Networks for Image Based Surface Reconstruction: An Investigation of Optimum Survey Designs Using UAV Derived Imagery and Structure-from-Motion Photogrammetry, *Remote Sensing*, 8, 1–8, 2016.
Waldhauser, F., and Ellsworth, W. L.: A Double-Difference Earthquake Location Algorithm: Method and Application to the Northern Hayward Fault, California, *Bulletin of the Seismological Society of America*, 90, 1353-1368, 10.1785/0120000006
190 %J *Bulletin of the Seismological Society of America*, 2000.

Waldhauser, F.: HypoDD: A Computer Program to Compute Double-difference Hypocenter Locations, USGS Open File Report 25, 1–113, 2001.

Williams, R.: Section 3.2 DEMs of difference. In: *Geomorphological Techniques (Online Edition)*, Clarke, L. E., and Nield, J. M. (Eds.), 2, British Society for Geomorphology, London, 2012.

195 Zhang, W., Qi, J., Wan, P., Wang, H., Xie, D., Wang, X., and Yan, G.: An Easy-to-Use Airborne LiDAR Data Filtering Method Based on Cloth Simulation, *Remote Sensing*, 8, 501, 2016.